

Charge orders in fully intercalated bilayer TaSe₂: Dependence on interlayer stacking and intercalation sites

Yuhui Yan,¹ Lingxiao Xiong,¹ and Feipeng Zheng^{1,*}

¹*College of Physics & Optoelectronic Engineering,
Department of Physics, Jinan University, Guangzhou 510632, China*

(Dated: May 30, 2025)

Recent advancements have established self-intercalation as a powerful technique for manipulating quantum material properties, with precise controllable intercalation concentrations. Given the inherently rich phase diagrams of transition metal dichalcogenides (TMDCs), studying the self-intercalated TMDCs can offer promising candidates for investigating the interplay between various orderings. This work focuses on fully intercalated bilayer TaSe₂ (Ta₃Se₄), which has recently been fabricated experimentally. By performing first-principles calculations, we demonstrate the suppression of an intrinsic 3×3 charge density wave (CDW) in parent TaSe₂ layers, and emergence of 2×2 , $\sqrt{3} \times \sqrt{3}$, or absence of a CDW in the intercalated layers, depending on the stacking sequence and intercalation sites being occupied. Particularly, the 2×2 CDW shows an increase in electronic states at the Fermi level compared to its non-CDW phase. This unusual behavior contrasts with that of typical CDW materials in TMDCs. Furthermore, superconductivity is preserved in these Ta₃Se₄ structures, with superconducting transition temperatures comparable to those of TaSe₂. Spin-orbit coupling is found to enhance the density of states at Fermi levels while simultaneously reducing the electron-phonon coupling matrix elements. These two competing effects result in varying impacts on superconductivity across different Ta₃Se₄ structures. Moreover, our calculations indicate that magnetic order is absent. Our study deepens the understanding of underlying physics in Ta₃Se₄, and provides experimentally feasible candidates for studying CDW, superconductivity, and their interplay.

I. INTRODUCTION

Transition metal dichalcogenides (TMDCs) have attracted considerable attention due to their rich electronic phase diagrams. Recent studies suggest that adjusting interlayer coupling offers an effective approach to tailoring the properties of layered materials. For example, by intercalating molecules into the interlayer space of bulk $2H$ -NbSe₂, it is possible to retain its high superconducting transition temperature while simultaneously exhibiting the Ising superconductivity characteristic of its monolayer counterpart [1, 2]. Additionally, when alkali metal atoms are intercalated into the interlayers of transition metal compounds, these systems can transform from ordinary metals [3–7] or semiconductors [8–10] into superconductors, with relatively high superconducting transition temperatures (T_c) or exhibiting Ising superconductivity. Furthermore, a transition from indirect to direct band gap semiconductor can be realized by eliminating the interlayer coupling in $2H$ -MoS₂ [11].

Recently, the intercalation of transition metal atoms can be realized with controllable intercalation concentrations by atomic diffusion in heterostructures [12], ionic liquid gating [13], or adjusting the relative chemical potential between metal and non-metal atoms [14–17], which provides new insights for tuning material properties. When the intercalants belong to the internal component in TMDCs, these systems are referred to as self-intercalated TMDCs. The experimental and theoretical results indicate that full self-intercalation (100%) significantly enhances superconductivity in PdTe₂ [12,

13]. Magnetic ordering can be induced in heteroatoms-intercalated layered materials, as demonstrated by experimental results, particularly resulting in the anisotropy-stabilized long-range ferromagnetism in Fe-intercalated TaS₂ [17]. Furthermore, theoretical calculations suggest that self-intercalated $2H$ -TaS₂ systems can exhibit intercalation-concentration-dependent magnetic orders [14], as well as distinct CDW orders from those of their parent materials [8], and can also switch between different structure phases when subjected to strains [8]. For $2H$ -TaSe₂, a sister compound of TaS₂, researchers have observed a $\sqrt{3} \times \sqrt{3}$ charge density modulation in a fully self-intercalated TaSe₂, using scanning transmission electron microscopy [14]. Considering that pristine TaSe₂ is a nonmagnetic system exhibiting coexistence of CDW and superconductivity, with T_c s and CDW transition temperatures (T_{CDWs}) measured at approximately 0.1–0.15 K and 120–122 K [18–23], respectively, the aforementioned observation raises the following questions: (1) Does the charge density modulation observed experimentally accompany a structure distortion? If so, what is the crystal structure of the distorted phase, and is the CDW enhanced or suppressed compared to pristine TaSe₂? (2) How does self-intercalation affect superconductivity? (3) Besides the experimentally observed structure, are there other competing structures for fully self-intercalated TaSe₂? (4) Considering that Ta is a heavy element, what is the effect of spin-orbit coupling (SOC) in this system?

In this work, we will computationally show multiple charge orders in fully intercalated bilayer TaSe₂ (Ta₃Se₄).

Ta₃Se₄ crystals can exhibit either the coexistence of $\sqrt{3} \times \sqrt{3}$, 2×2 , and 2×1 CDWs with superconductivity, or superconductivity alone, depending on the interlayer stacking order and the occupied intercalation sites in the interlayer space. In particular, our calculations accurately reproduce the experimentally observed Ta₃Se₄ crystal, which exhibits a specific crystal structure featuring a $\sqrt{3} \times \sqrt{3}$ CDW. We further show that this structure can host superconductivity with a T_c comparable to that of its parent material. Furthermore, we find that the self-intercalation generally leads to the suppression of 3×3 CDW in parent TaSe₂, with an enhanced or an absent CDW in intercalation layers. SOC is found to play diverse roles in the superconductivity of various Ta₃Se₄ crystals, exhibiting effects ranging from suppression and enhancement to negligible impact. The underlying mechanisms behind these results are revealed through calculations of formation energies, electronic structures, harmonic and anharmonic phonons, electron-phonon coupling (EPC), and superconducting properties.

II. COMPUTATIONAL METHODS

First-principles density functional theory (DFT) calculations were conducted using projector-augmented-wave (PAW) [24] and ultrasoft pseudopotential [25], combined with the PBEsol [26] exchange-correlation functional. These calculations employ a combination of the Quantum Espresso (QE) [27–29] and Vienna Ab Initio Simulation Package (VASP) [30] software packages. The VASP package is used for calculating the unfolded band structures and Fermi surfaces, as well as magnetic properties, while the remaining calculations are performed using the QE. We focus on three crystal structures of Ta₃Se₄, named $1H_{\text{hollow}}$ -Ta₃Se₄, $2H_{\text{Ta}}$ -Ta₃Se₄, and $1H_{\text{Ta}}$ -Ta₃Se₄, respectively, which are defined later in the main text. The PAW pseudopotentials were used for the calculations of $1H_{\text{hollow}}$ -Ta₃Se₄ and $1H_{\text{Ta}}$ -Ta₃Se₄, while the ultrasoft pseudopotentials were used for $2H_{\text{Ta}}$ -Ta₃Se₄. The reasons for the above choices can be found in Sec. S1 [31]. To simulate the thin-film geometry and reduce interactions between periodic boundaries, a vacuum layer of approximately 15 Å is introduced. The Kohn-Sham valence states are expanded using plane waves, with energy cutoffs set at 50 Ry and 500 Ry for wave functions and charge densities, respectively. Structural optimizations are carried out until the Hellmann-Feynman force acting on each atom is less than 1×10^{-5} Ry/Bohr. An $18 \times 18 \times 1$ \mathbf{k} -grid and a $6 \times 6 \times 1$ \mathbf{q} -grid are used to calculate the ground states of charge densities and phonons, respectively, for non-CDW Ta₃Se₄ and Ta₂Se₄. These grids are scaled for the calculation of CDW Ta₃Se₄ and Ta₂Se₄, according to the sizes of their respective CDW supercells. The electron-phonon coupling (EPC) matrix elements $g_{mn,\nu}(\mathbf{k}, \mathbf{q})$ are first computed [49–52] based on

the above \mathbf{k} and \mathbf{q} grids, where m and n are band indices, and ν indicates a phonon branch. The matrix elements quantify the scattering amplitude between the electronic states with a wave vector \mathbf{k} , a band index m [denoted as (\mathbf{k}, m)], and $(\mathbf{k} + \mathbf{q}, n)$ through a phonon mode with a branch ν and a wave vector \mathbf{q} . Then the matrix elements are further interpolated [51] to a $180 \times 180 \times 1$ \mathbf{k} -grid and a $60 \times 60 \times 1$ \mathbf{q} -grid, whereby the Eliashberg function $\alpha^2 F(\omega)$ is calculated. The $\alpha^2 F(\omega)$ is defined as

$$\alpha^2 F(\omega) = \frac{1}{2} \sum_{\nu} \int_{\text{BZ}} \frac{d\mathbf{q}}{\Omega_{\text{BZ}}} \omega_{\mathbf{q}\nu} \lambda_{\mathbf{q}\nu} \delta(\omega - \omega_{\mathbf{q}\nu}), \quad (1)$$

where $\lambda_{\mathbf{q}\nu}$ is a phonon-momentum-resolved EPC constant, and Ω_{BZ} is the volume of the first Brillouin Zone (BZ). The Dirac delta function $\delta(\omega - \omega_{\mathbf{q}\nu})$ is approximated by a Gaussian function with a broadening of 0.5 meV. The total EPC constants are obtained by

$$\lambda = 2 \int \frac{\alpha^2 F(\omega)}{\omega} d\omega. \quad (2)$$

This quantity can be effectively represented as $\lambda = 2N(0)\langle |g|^2 \rangle / \omega_0$, where $N(0)$ is a density of states at Fermi level, and $\langle |g|^2 \rangle$ is an average of the EPC matrix elements on Fermi surface, which can be estimated by $\langle |g|^2 \rangle = \frac{1}{N(0)} \int \alpha^2 F(\omega) d\omega$ [53]. The superconducting T_c is calculated by McMillan-Allen-Dynes approach [54], defined as

$$T_c = \frac{\omega_{\log}}{1.2} \exp \left(- \frac{1.04(1 + \lambda)}{\lambda - \mu^*(1 + 0.62\lambda)} \right), \quad (3)$$

where ω_{\log} is a logarithmic average of phonon frequencies $\omega_{\log} = \exp[\frac{2}{\lambda} \int_0^\infty d\omega \frac{\alpha^2 F(\omega)}{\omega} \log \omega]$. μ^* is the Morel-Anderson Coulomb potential, which is set to be 0.15, a typical value for TMDCs [55–57]. The temperature-dependent electron-momentum-resolved superconducting gaps on the Fermi surface, denoted as $\Delta(\mathbf{k}, T)$, were determined by solving the anisotropic Migdal-Eliashberg equations on an imaginary axis and then analytically continuing to the real axis using Padé functions [58]. In solving these equations, the Kohn-Sham states within 100 meV of the Fermi level are included, and the Matsubara frequencies are cut off at 0.35 eV, which are sufficient to describe the EPC in this system.

Anharmonic phonon calculations are performed using the stochastic self-consistent harmonic approximation (SSCHA) [59–61], a non-perturbative method that accounts for anharmonicity arising from both thermal and quantum fluctuations. A 3×3 supercell containing 63 atoms are chosen, which is commensurate with the \mathbf{q}_{CDW} of $1H_{\text{hollow}}$ -Ta₃Se₄. We use a number of 2000 configurations in each population to obtain converged free energy Hessian. Machine learning potentials, developed using the deep potential molecular dynamics method [62, 63], are employed to model atomic interactions at various

temperatures, enabling more efficient computation of the configurations in each population. The training sets comprise DFT-calculated energies, forces, and external pressures for one thousand configurations generated by SSCHA in each temperature. The DFT calculations are performed with the same precision as the electronic structure calculations described earlier. To achieve optimal concordance between DFT-computed properties and those predicted by the machine learning potential, the loss function—encompassing energy, force, and external pressure contributions—undergoes minimization through four million iterative optimization steps. A comparative analysis of energies, forces, and external pressures derived from DFT calculations and machine learning potential predictions shown in Sec. S2 [31].

The unfolded band structures and Fermi surfaces calculations are performed using the same method as our previous works [64, 65].

III. RESULTS AND DISCUSSIONS

A. Property of TaSe₂ without intercalation

Before studying Ta₃Se₄, we first calculate the properties of TaSe₂ using various types of pseudopotentials to identify the most suitable computational methods for this system, as shown in Sec. S3 [31]. We find that using PAW pseudopotentials ([24]) with an exchange-correlation functional of PBEsol leads to the calculated hexagonal lattice constants $a = 3.41$ Å, and $c = 12.63$ Å, which closely match the experiments [66] with a maximum error of 0.32 %. The calculated electronic band structure for monolayer TaSe₂ displays a hole (electron) pocket centered at the Γ (K) point, which is consistent with previous studies [66–71]. Furthermore, the calculated $\omega_{\mathbf{q}\nu}$ of bilayer TaSe₂, shown in Sec. S4 [31], exhibits the most negative phonon frequency at $\mathbf{q} = 2/3\mathbf{K}$, suggesting a 3×3 CDW instability, consistent with experimental measurements [18, 67, 72]. The above results suggest our computational method is valid to describe the properties in TaSe₂ systems.

B. Three candidate crystal structures of Ta₃Se₄

Following the intercalation of Ta, it is essential to determine the crystal structure of Ta₃Se₄, as the intercalant can potentially occupy multiple sites in the interlayer space, and the intercalation process may alter the stacking sequence between adjacent TaSe₂ layers. We construct initial structural models that incorporate various stacking sequences (Sec. S5 [31]) and consider typical intercalation sites within the interlayer space. After structure optimizations, we obtain 12 different structures, whose total energies are shown in Sec. S6 [31]. We

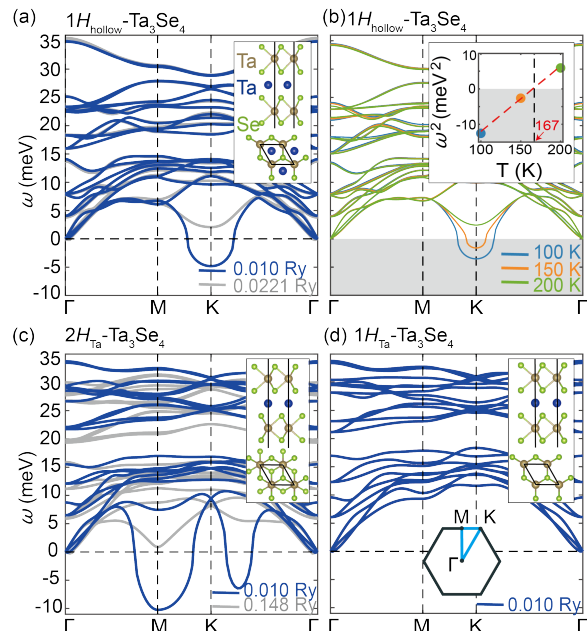


FIG. 1. Calculated phonon dispersions under harmonic approximation for (a) $1H_{\text{hollow}}\text{-Ta}_3\text{Se}_4$, (c) $2H_{\text{Ta}}\text{-Ta}_3\text{Se}_4$, and (d) $1H_{\text{Ta}}\text{-Ta}_3\text{Se}_4$ in non-CDW phases, respectively, using different values of electron broadening. The insets in the above panels show the side and top views of the corresponding structures. (b) Anharmonic phonon spectra calculated from the SSCHA free energy Hessian at several temperatures for non-CDW $1H_{\text{hollow}}\text{-Ta}_3\text{Se}_4$. The inset presents a linear fit of the squared phonon energies at the K point across different temperatures.

found that two structures exhibit a tiny total energies difference of 13 meV/f.u., and their energies are substantially lower than those of the other structures. Their calculated phonon dispersions ($\omega_{\mathbf{q}\nu}$ s) and corresponding crystal structures are shown in Figs. 1(c) and 1(d), respectively. We refer to the former structure, shown in Fig. 1(c), as $2H_{\text{Ta}}\text{-Ta}_3\text{Se}_4$, since it features the $2H$ interlayer stacking between two TaSe₂ layers, and the occupied intercalation sites aligned with the parent Ta atoms in the out-of-plane direction. The latter one is referred to as $1H_{\text{Ta}}\text{-Ta}_3\text{Se}_4$, since it manifests the same occupied intercalation sites but with $1H$ interlayer stacking (Fig. 1(d)). Upon further examination of the remaining structures, we found that one of them exhibits the same structural features as experimentally measured Ta₃Se₄ by scanning tunneling electronic microscopy [14], but with a higher calculated energy of approximately 1.26 eV/f.u. related to $2H_{\text{Ta}}\text{-Ta}_3\text{Se}_4$ or $1H_{\text{Ta}}\text{-Ta}_3\text{Se}_4$. As shown in Fig. 1(a), this structure is characterized by the $1H$ interlayer stacking and the occupied intercalation positions at the hollow sites, which we refer to as $1H_{\text{hollow}}\text{-Ta}_3\text{Se}_4$. Thus, although $1H_{\text{hollow}}\text{-Ta}_3\text{Se}_4$ theoretically exhibits a higher total energy compared to both $1H_{\text{Ta}}\text{-}$, and $2H_{\text{Ta}}\text{-Ta}_3\text{Se}_4$, it can still be synthesized.

This is reminiscent of the synthesis of $2M\text{-WS}_2$, which has a much higher energy than $2H\text{-WS}_2$ [73, 74]. The above results suggest the possibility of multiple structural phases in Ta_3Se_4 , warranting further experimental validation. Thus, the following discussions will focus on the three Ta_3Se_4 structures: $1H_{\text{hollow-}}$, $1H_{\text{Ta-}}$, and $2H_{\text{Ta-}}\text{-Ta}_3\text{Se}_4$. The spin spiral calculations, as shown in Sec. S7 [31], suggest that all the three structures are non-magnetic, similar to the cases of fully intercalated TaS_2 in bilayer [14, 56] and bulk phases [14].

C. Property of $1H_{\text{hollow-}}\text{-Ta}_3\text{Se}_4$

We begin with the analysis of lattice dynamics of $1H_{\text{hollow-}}\text{-Ta}_3\text{Se}_4$. The calculated $\omega_{\mathbf{q}\nu}$, as shown in Fig. 1(a), reveals the most negative phonon energy of -4.83 meV at the K point, indicating a potential $\sqrt{3} \times \sqrt{3}$ CDW instability in the undistorted $1H_{\text{hollow-}}\text{-Ta}_3\text{Se}_4$ crystal. This is in excellent agreement with the experimental measurement [14], where the same CDW order has been detected. Furthermore, we find that the frequency of the imaginary phonons is sensitive to the electronic broadening, indicating that they are associated with Kohn anomalies driven by EPC [75]. As shown in Fig. 1(a), slightly increase the electronic broadening from a regular value of 0.01 Ry to 0.022 Ry, eliminates those imaginary phonons. This value of electronic broadening is slightly higher than that of bilayer TaSe_2 (0.021 Ry) as shown in Sec. S4 [31], implying a possible higher T_{CDW} in $1H_{\text{hollow-}}\text{-Ta}_3\text{Se}_4$. To accurately determine T_{CDW} , it is essential to move beyond the harmonic approximation. This is achieved by considering both quantum ionic fluctuations and thermal anharmonic fluctuations at finite temperatures, utilizing SSCHA [59–61]. The calculated $\omega_{\mathbf{q}\nu}$ s for $1H_{\text{hollow-}}\text{-Ta}_3\text{Se}_4$ at temperatures of 100, 150 and 200 K using SSCHA are shown in Fig. 1(b). As the temperature increases, the $\omega_{\mathbf{q}\nu}$ s demonstrate a gradual hardening of the imaginary phonons around the K point, while the other phonon frequencies remain nearly unchanged. By a linear fit of the $\omega_{\mathbf{q}\nu}^2$ at the K point, the T_{CDW} is estimated to be 167 K as shown in the inset of Fig. 1(b). The value of T_{CDW} is slightly higher than that of monolayer and bilayer TaSe_2 , which are measured to be approximately 130 K [76, 77] and 120 K [18, 19, 21, 22], respectively. This is consistent with the relatively smaller CDW formation energy, and more pronounced deformation of Ta-Ta distances in CDW $1H_{\text{hollow-}}\text{-Ta}_3\text{Se}_4$, which will be discussed later.

To further investigate the CDW structure associated with the imaginary phonon, we construct $\sqrt{3} \times \sqrt{3}$ supercells with random atomic displacements relative to the equilibrium positions. After multiple structure optimizations, we obtain one structure with an energy of -4.95 meV/f.u. related to its non-CDW state. This energy gain is larger than that of bilayer TaSe_2 , calculated at

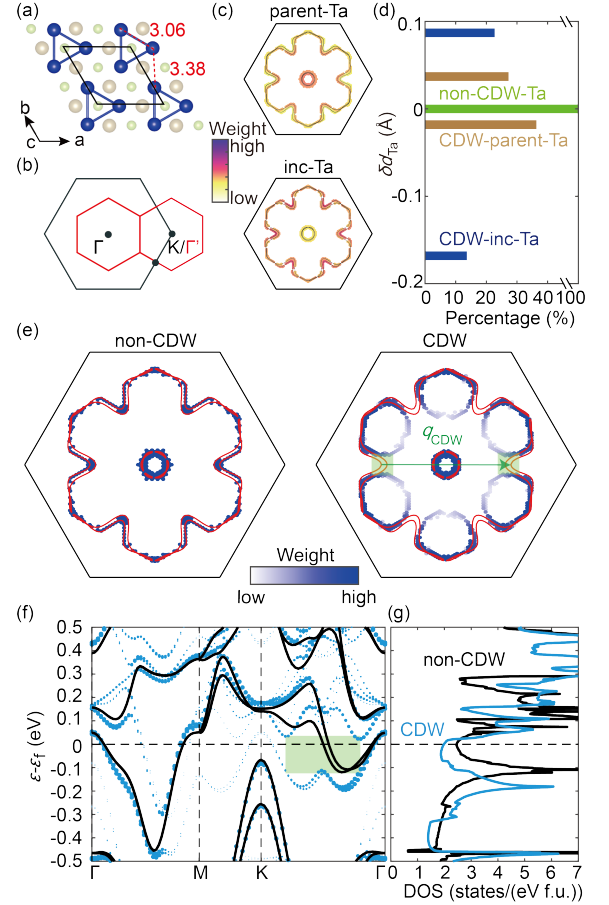


FIG. 2. Crystal and electronic structure of $1H_{\text{hollow-}}\text{-Ta}_3\text{Se}_4$. (a) Top view of its $\sqrt{3} \times \sqrt{3}$ CDW structure, where the intercalation layer is highlighted. The solid lines between Ta atoms in the intercalation layer indicate that their distance decreases relative to that in non-CDW structure. More details can be found in Sec. S8 [31]. (b) BZs for non-CDW (black) and CDW (red) phases, with corresponding high symmetry points. (c) Projected electronic states around the Fermi surface onto Ta atoms in the parent TaSe_2 (parent-Ta) and intercalation layer (inc-Ta). (d) The distribution of δd_{Ta} in CDW $1H_{\text{hollow-}}\text{-Ta}_3\text{Se}_4$, showing the change of Ta-Ta distances compared to those in non-CDW phase that of its non-CDW phase. (e) Unfolded Fermi surfaces of non-CDW and CDW $1H_{\text{hollow-}}\text{-Ta}_3\text{Se}_4$ in primitive BZs. The green rectangular sections highlight two gapped regions that are related by \mathbf{q}_{CDW} . Only the states within an energy window of ± 21 meV are shown. The solid lines represent the directly calculated Fermi surface of non-CDW structure. (f) The unfolded band structure of CDW $1H_{\text{hollow-}}\text{-Ta}_3\text{Se}_4$ in primitive BZ, overlaid with the directly calculated band structure of the non-CDW phase, represented by black lines. (g) DOS for non-CDW and CDW phases.

-3.88 meV/f.u., aligning with the calculated larger T_{CDW} in $1H_{\text{hollow-}}\text{-Ta}_3\text{Se}_4$ as mentioned before. The calculated $\omega_{\mathbf{q}\nu}$ shown in Fig. 3(c) indicates dynamical stability of the reconstructed structure, as all the imaginary phonons were removed after the atomic reconstruction. This sug-

gests that the reconstructed structure is likely to be a CDW structure induced by the phonon instability at the K point. By further examination of the $\sqrt{3} \times \sqrt{3}$ CDW structure, we find that the largest deviation of the Ta-Ta distances compared to that of its non-CDW structure (δd_{Ta}) in the intercalation layer is -0.17 \AA , as shown in Fig. 2(d). In contrast, the δd_{Ta} in parent layer reduces from 0.16 \AA to 0.04 \AA after the intercalation. This indicates that after the Ta intercalation, the 3×3 CDW in parent TaSe_2 layers is suppressed, and the $\sqrt{3} \times \sqrt{3}$ CDW is emergent in the intercalated Ta layer, reminiscent of similar behavior in Ta_3S_4 [56]. The modification of the Ta-Ta distances after the intercalation results in the formation of trimers within the intercalation layer, which are centered at Se atoms from the top view, as shown in Fig. 2(a).

Furthermore, it is crucial to understand the effect of CDW on the electronic structure. The non-CDW $1H_{\text{hollow}}\text{-Ta}_3\text{Se}_4$ exhibits a metallic band structure with two bands crossing Fermi level along Γ -M and Γ -K paths as shown by solid lines in Fig. 2(f). This leads to the formation of two small, degenerate hole pockets and two large electron pockets centered at the Γ point (Fig. 2(e)). These Fermi pockets are associated with the hybridization of electronic states from the parent and intercalated Ta atoms with varying mixing ratios, as shown in Fig. 2(c). The two inner pockets are primarily contributed by parent Ta atoms, with intercalated Ta atoms playing a secondary role. The two outer pockets exhibit an opposite behavior. By comparing the band structure of non-CDW $1H_{\text{hollow}}\text{-Ta}_3\text{Se}_4$ to the unfolded band structure of CDW $1H_{\text{hollow}}\text{-Ta}_3\text{Se}_4$ (blue dots), it is clear that the most notable change near Fermi level is gaps opening with a size of approximately 0.13 meV along the Γ -K path, as highlighted in Fig. 2(f). This leads to the development of gaps around the Fermi surface near the wave vectors $1/2\text{K}$ ($1/2\text{K}'$), as demonstrated through a comparison of the Fermi surfaces: in the CDW phase, the unfolding weights near these wave vectors vanish (Fig. 2(e)), whereas the non-CDW phase exhibits a uniform distribution of the weights with large values along the directly calculated Fermi surface (red solid lines). This leads to the reduction of $N(0)$ from 2.46 /eV/f.u. in non-CDW phase to 1.98 /eV/f.u. in CDW phase. The formation of the gaps near $1/2\text{K}$ ($1/2\text{K}'$) is reasonable, as the \mathbf{k} states in different gapped regions are related by \mathbf{q}_{CDW} , as indicated in Fig. 2(e). For example, the gapped regions highlighted in Fig. 2(e) are connected by a wave vector of $2/3\mathbf{a}^* - 1/3\mathbf{b}^*$, which corresponds to one of the CDW vectors (see Sec. S13 [31] for details). This observation is similar to other CDW materials in H -type TMDCs, where the CDWs lead to the partial gap opening at Fermi level and reduce $N(0)$ to some extents [56, 64, 65, 69, 70, 78]. The above results demonstrate that the primary effect of CDW is to open energy gaps around Fermi surface near the wave vectors of the $1/2\text{K}$

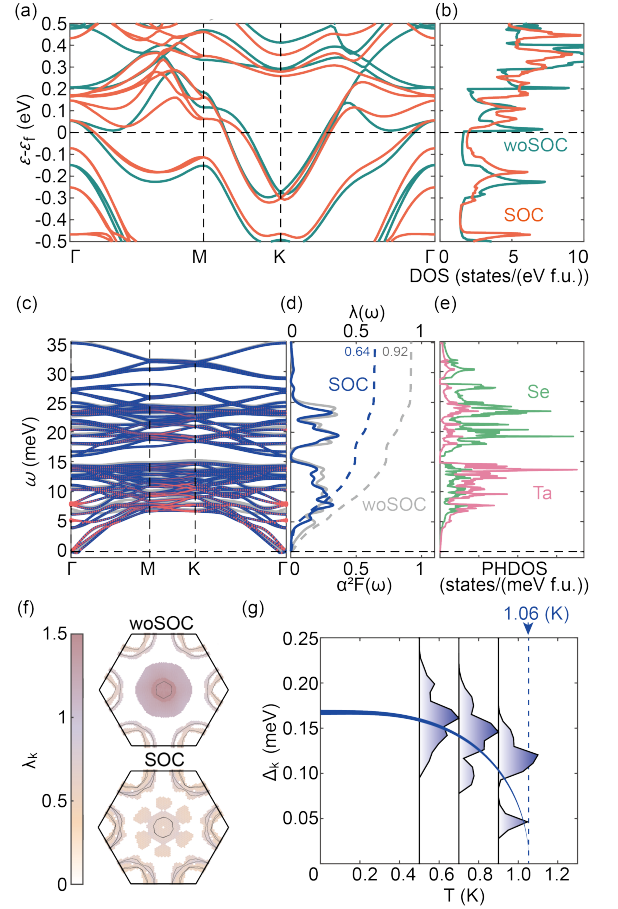


FIG. 3. The electronic properties and phonons of $1H_{\text{hollow}}\text{-Ta}_3\text{Se}_4$ in the $\sqrt{3} \times \sqrt{3}$ CDW phase. The band structure (a) and DOS (b) of CDW $1H_{\text{hollow}}\text{-Ta}_3\text{Se}_4$, calculated with and without SOC. (c) $\omega_{\mathbf{q}\nu}$ with (blue) and without (grey) SOC. The size of red dots represents the value of $\lambda_{\mathbf{q}\nu}$ in the presence of SOC. (d) $\alpha^2 F(\omega)$ along with $\lambda(\omega)$, calculated with and without SOC. (e) Projected phonon density of states (PHDOS) onto the vibrations of Se and Ta atoms. (f) Distribution of \mathbf{k} -resolved EPC constants near the Fermi surface in the presence of SOC. Only the states within an energy window of $\pm 55 \text{ meV}$ are shown. (g) Histograms of $\Delta(\mathbf{k}, T)$ at various temperatures. The blue curve represents a BCS fit of the energy gap.

($1/2\text{K}'$) points, leading to the reduced $N(0)$.

With the formation of gaps near the Fermi surface, a natural question arises: can superconductivity exist in CDW $1H_{\text{hollow}}\text{-Ta}_3\text{Se}_4$? As shown in Fig. 3(d), the λ of this system is calculated to be 0.64 with the inclusion of SOC. Combined with the calculated $\omega_{\text{log}} = 110.92 \text{ K}$, the McMillan T_c (T_c^{ME}) is estimated at 1.79 K . Further consideration of the anisotropic EPC properties reveals a single gap structure of $\Delta(\mathbf{k}, T)$, as shown in Fig. 3(g). The $\Delta(\mathbf{k}, T)$ is predicted to vanish at 1.06 K , indicating the anisotropic Migdal-Eliashberg T_c (T_c^{aniso}) around this value. Furthermore, given that anharmonic effects may significantly impact the electron-phonon coupling [79],

we conducted further calculations on the electron-phonon coupling properties taking anharmonicity into account. We found that both the phonon and $\alpha^2F(\omega)$ spectra remain nearly unchanged after accounting for anharmonicity, as shown in Sec. S9 [31]. This observation aligns with an experimental measurement indicating that the anharmonicity in layered TaSe₂ is weak [80]. According to previous studies, the T_c in TaSe₂ increases when going from bulk to monolayer limit within a range of 0.1–1.8 K [18–20, 57, 81–83], as tabulated in Tab. I. Thus, our result indicates that the superconductivity in $1H_{\text{hollow}}\text{-Ta}_3\text{Se}_4$ can coexist with the $\sqrt{3} \times \sqrt{3}$ CDW order, with comparable T_c to its parent materials without intercalation.

We also note that the SOC tends to suppress superconductivity in CDW $1H_{\text{hollow}}\text{-Ta}_3\text{Se}_4$, according to the results of both isotropic (Fig. 3(d)) and anisotropic (Fig. 3(g) and Sec. S10 [31]) EPC calculations. For example, the calculated λ with and without SOC are 0.64 and 0.92, respectively. It is also worth noting that SOC slightly increases $N(0)$ from 1.65 eV/f.u. to 1.98 eV/f.u., as shown in Fig. 3(b). Thus, the reduction in λ is likely attributed to a decrease in the EPC matrix elements induced by SOC. This is indeed the case, as incorporating SOC reduces the estimated average of the squared EPC matrix elements (see “Computational Methods”) from 2820 to 1850 meV². Furthermore, a comparison of the $\alpha^2F(\omega)$ between the two cases, as shown in Fig. 3(d), clearly indicates that the reduction in λ originates from the diminished contribution of phonons in the 0–15 meV energy range. These phonon states are related to the Ta vibrations as shown in Fig. 3(e). The above results indicated that the reduced EPC matrix elements are primarily associated with the vibrations of Ta atoms.

D. Property of $2H_{\text{Ta}}\text{-Ta}_3\text{Se}_4$

The calculated $\omega_{q\nu}$ for pristine $2H_{\text{Ta}}\text{-Ta}_3\text{Se}_4$, as shown in Fig. 1(c), indicates that the most negative phonon energy occurs at the M point, with the second most negative energy appearing at the wave vector of $3/4K$. This suggests the competing CDW orders associated with the above two wave vectors. Interestingly, an significantly large electron broadening of 0.148 Ry is needed to remove these imaginary phonons as shown in Fig. 1(c), which is much larger than that of $2L\text{-TaSe}_2$ (0.021 Ry) and $1H_{\text{hollow}}\text{-Ta}_3\text{Se}_4$ (0.022 Ry), suggesting a much higher T_{CDW} in $2H_{\text{Ta}}\text{-Ta}_3\text{Se}_4$. This is similar to the case of $2H_{\text{Ta}}\text{-Ta}_3\text{S}_4$, where a 0.08 Ry electron broadening is required [56].

As temperature decreases, the CDW transition is expected to initiate at the M points, due to the most negative phonon energy at these points. Thus, we construct 2×2 supercells to study the corresponding CDW distortion. After multiple structure optimizations, we ob-

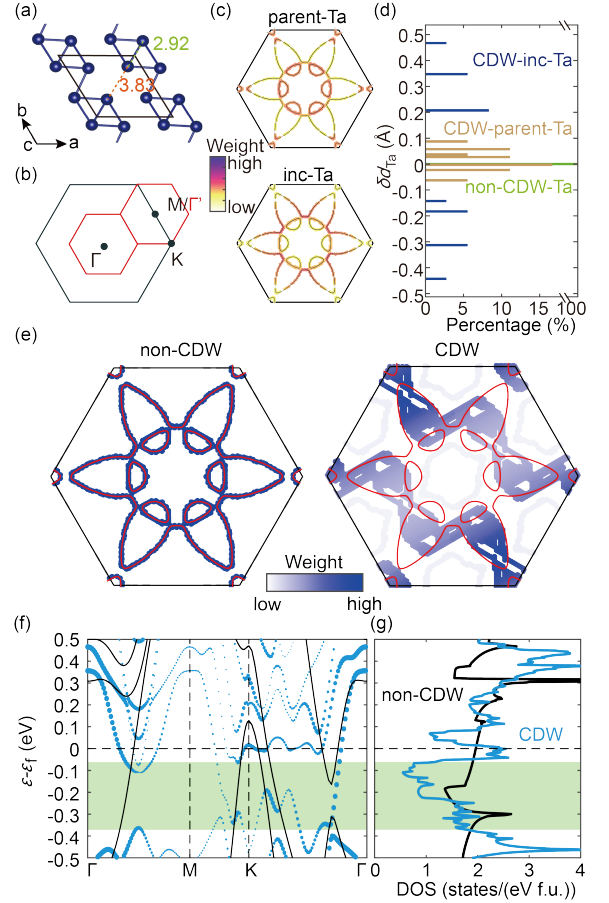


FIG. 4. Crystal and electronic structure of $2H_{\text{Ta}}\text{-Ta}_3\text{Se}_4$. (a) Top view of the intercalation layer in 2×2 CDW structure. More details can be found in Sec. S8 [31]. (b) BZs for non-CDW (black) and CDW (red) phases. (c) Projected electronic states around the Fermi surface onto parent-Ta and inc-Ta atoms. (d) The distribution of δd_{Ta} in CDW $2H_{\text{Ta}}\text{-Ta}_3\text{Se}_4$. (e) Unfolded Fermi surfaces of the non-CDW and CDW phases in primitive BZ. In panels (c) and (e), only the states within an energy window of ± 35 meV are shown. The solid lines are the directly calculated Fermi surface of the non-CDW phase. (f) The unfolded band structure of the CDW phase in primitive BZ, overlaid with the directly calculated band structure of the non-CDW phase, represented by black lines. (g) DOS for non-CDW and CDW phases. The shaded areas in panels (f) and (g) highlight the energy ranges where band gaps emerge as a consequence of CDW formation.

tain a reconstructed structure with a total energy 47.45 meV/f.u. lower than non-CDW $2H_{\text{Ta}}\text{-Ta}_3\text{Se}_4$. This energy difference is an order of magnitude larger than that in the case of $1H_{\text{hollow}}\text{-Ta}_3\text{Se}_4$. The calculated $\omega_{q\nu}$, shown in Fig. 5(c), suggests the dynamical stability of this structure, as all $\omega_{q\nu}$ values are positive, except for a small region near the Γ point with negligible negative energies. This suggests that the reconstructed structure is the CDW structure associated with the phonon instability at the M points. The above result implies the CDW instability associated with $3/4K$ is completely suppressed

after the formation of the CDW relative to the M points.

Upon further analysis, the distribution of δd_{Ta} shows a behavior akin to that of $1H_{\text{hollow}}\text{-Ta}_3\text{Se}_4$, as depicted in Fig. 4(d): the CDW distortion is suppressed in parent TaSe_2 , while enhanced in the intercalation layer, with δd_{Ta} being less than 0.09 Å in the former and reaching 0.47 Å in the latter. This δd_{Ta} value is much larger than that of $1H_{\text{hollow}}\text{-Ta}_3\text{Se}_4$ (0.17 Å), consistent with the much larger T_{CDW} in $2H_{\text{Ta}}\text{-Ta}_3\text{Se}_4$, as previously analyzed. The formation of the δd_{Ta} leads to a significant structure distortions relative to its non-CDW state in the intercalation layer, as shown in Fig. 4(a). The structure manifests quasi-one-dimensional Ta-Ta chains running along the direction of a lattice vector \mathbf{b} as shown in Fig. 4(a) (or its symmetry-equivalent directions). Each of the chain consists of edge-shared triangles connected along the $\mathbf{a} + \mathbf{b}$ direction. The above atomic reconstruction leads to the formation of 2×2 CDW structure in $2H_{\text{Ta}}\text{-Ta}_3\text{Se}_4$. The main characteristic of the CDW $2H_{\text{Ta}}\text{-Ta}_3\text{Se}_4$ is similar to $2H_{\text{Ta}}\text{-Ta}_3\text{S}_4$, both featuring quasi-one-dimensional Ta-Ta chains in the intercalation layer [56]. However, the chains in $2H_{\text{Ta}}\text{-Ta}_3\text{S}_4$ are formed in 2×1 supercells in strain-free case. In Sec. S11 [31], we show that compressive strains tend to gradually suppress CDW in $2H_{\text{Ta}}\text{-Ta}_3\text{Se}_4$. By applying a 2% compressive strains, the system can transform from the 2×2 CDW state into a 2×1 CDW state. Further increasing the strain to 5.4% will eliminate the CDW instability, triggering a transition to a non-CDW phase. In contrast, tensile strains further stabilize and enhance the 2×2 CDW order. The above results indicate a rich structure phase diagram in $2H_{\text{Ta}}\text{-Ta}_3\text{Se}_4$.

Due to the significant CDW distortions discussed above, the electronic structure in the CDW phase undergoes substantial changes. Interestingly, we found that the CDW increases the $N(0)$ in $2H_{\text{Ta}}\text{-Ta}_3\text{Se}_4$, contrasting with the commonly observed phenomenon in TMDCs. As shown in Fig. 4(g), $N(0)$ exhibits a clear increase from 1.96 eV/f.u. in non-CDW $2H_{\text{Ta}}\text{-Ta}_3\text{Se}_4$ to 2.46 eV/f.u. in its CDW phase. A further comparison of the DOS between the non-CDW and CDW phases reveals that the gap opening due to the CDW occurs primarily in the energy range of approximately -0.36 to -0.06 eV, as highlighted in Fig. 4(g). This shifts the electronic states to energy levels on both sides adjacent to the gapped region, leading to the formation of the DOS peaks around the Fermi level (Fig. 4(g)). This is further rationalized by comparing the band structures of the non-CDW and CDW phases in primitive BZ as shown in Fig. 4(f), where the unfolding weights for the electronic states of the CDW phase are clearly reduced in the gapped energy region, and enhanced near Fermi level. A direct comparison of the number of electronic states near the Fermi level provides further support for the above conclusion, as shown in Fig. 4(e), where an increased number of states near the Fermi level can be observed in the

CDW phase. We also note that the symmetry of the Fermi surface in the CDW phase is reduced to C_2 symmetry compared to that in the non-CDW phase, which can be attributed to the breaking of C_3 symmetry in the CDW phase. A consistent result can also be obtained by comparing the band structures in supercell BZ, as shown in Sec. S12 [31], where the number of bands of the CDW phase is clearly reduced in the gapped energy region. Thus, we have shown that the energy gap formation in occupied states increases $N(0)$ in CDW $2H_{\text{Ta}}\text{-Ta}_3\text{Se}_4$. This is different from typical CDW materials in TMDCs (e.g., NbSe_2 , TaSe_2), where gaps form at the Fermi level, leading to the reduced $N(0)$ [56, 64, 65, 69, 70, 78]. The unusual behavior of CDW is reminiscent of monolayer VSe_2 , where unconventional CDW with the full gap in the unoccupied states were confirmed both experimentally and theoretically [84].

Although the CDW $2H_{\text{Ta}}\text{-Ta}_3\text{Se}_4$ exhibits enhanced $N(0)$ compared to its non-CDW phase, a weak EPC in this material leads to a small T_c^{ME} . According to the calculated $\alpha^2 F(\omega)$ and $\lambda(\omega)$, as shown in Fig. 5(d), λ of the system is only 0.48. Combined with the calculated $\omega_{\text{log}} = 109.06$ K, the T_c^{ME} in CDW $2H_{\text{Ta}}\text{-Ta}_3\text{Se}_4$ is estimated to be 0.39 K, which is clearly smaller than $1H_{\text{hollow}}\text{-Ta}_3\text{Se}_4$ (1.79 K), and monolayer TaSe_2 (1.8 K), as tabulated in Tab. I. Upon further comparison of $N(0)$ and λ among the materials listed in Tab. I, we find that while the $N(0)$ of $2H_{\text{Ta}}\text{-Ta}_3\text{Se}_4$ (2.46 /eV/f.u.) is comparable to that of monolayer TaSe_2 (2.46 /eV/f.u.) and $1H_{\text{hollow}}\text{-Ta}_3\text{Se}_4$ (1.98 /eV/f.u.), its λ is noticeably smaller. This can be attributed to the overall smaller EPC matrix elements in $2H_{\text{Ta}}\text{-Ta}_3\text{Se}_4$, as its estimated $\langle |g|^2 \rangle$ is only 1240 meV², which is substantially smaller than that of $1H_{\text{hollow}}\text{-Ta}_3\text{Se}_4$ (1850 meV²). We also find that SOC has minimal impact on the EPC and superconductivity in the CDW $2H_{\text{Ta}}\text{-Ta}_3\text{Se}_4$, reminiscent of similar behavior in CDW $2H_{\text{Ta}}\text{-Ta}_3\text{S}_4$ [56]. The calculated $\alpha^2 F(\omega)$ spectra are nearly identical with and without SOC (Fig. 5(d)), and the values of λ and T_c^{ME} show little variation with and without consideration of SOC, as listed in Tab. I. A further comparison of the values of $N(0)$ and $\langle |g|^2 \rangle$ calculated with and without SOC (see Tab. I) reveals that the SOC slightly increases $N(0)$ and decreases $\langle |g|^2 \rangle$. These two effects counterbalance each other, resulting in similar values of λ and T_c^{ME} . We further show in Fig. 5(a) that the enhancement of $N(0)$ induced by SOC is directly related to the band splitting near the Fermi level, which results in the formation of a locally flat band in the vicinity of the K point.

After the consideration of anisotropic EPC properties without SOC, the T_c^{aniso} is estimated at 1.34 K, as shown in Fig. 5(g), which is higher than its T_c^{ME} . The observed enhancement can be attributed to the anisotropic distribution of $\lambda_{\mathbf{k}}$, which exhibits relatively large values near the M points, as depicted in Fig. 5(f). The above analysis highlights the critical role of anisotropic EPC in

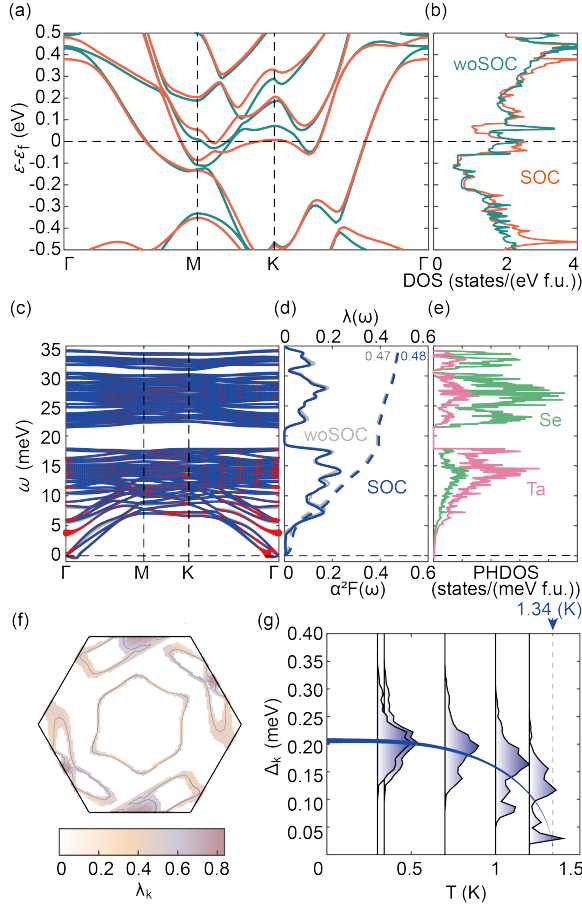


FIG. 5. The properties of $2H_{\text{Ta}}\text{-Ta}_3\text{Se}_4$ in the 2×2 CDW phase. The band structure (a) and DOS (b) of the CDW phase, calculated with and without SOC. (c) $\omega_{q\nu}$ with (blue) and without (grey) SOC. The size of red dots represents the value of $\lambda_{q\nu}$ in the presence of SOC. (d) $\alpha^2 F(\omega)$ along with $\lambda(\omega)$, calculated with and without SOC. (e) Projected PH-DOS onto the vibrations of Se and Ta atoms. (f) Distribution of \mathbf{k} -resolved EPC constants near the Fermi surface in the absence of SOC. Only the states within an energy window of ± 35 meV are shown. (g) Histograms of $\Delta(\mathbf{k}, T)$ at various temperatures in the absence of SOC. The blue curve represents a BCS fit of the energy gap.

determining the superconducting properties of this system. Furthermore, when SOC is introduced, the band structure shown in Fig. 5(a) suggests a redistribution of $\lambda_{\mathbf{k}}$: the values around the M points are expected to decrease, while those near the K points are anticipated to increase. However, due to the counterbalancing effects of these changes, T_c^{aniso} is likely to remain largely unaffected.

E. Property of $1H_{\text{Ta}}\text{-Ta}_3\text{Se}_4$

Interestingly, the calculated $\omega_{q\nu}$ for $1H_{\text{Ta}}\text{-Ta}_3\text{Se}_4$ as shown in Fig. 1(d) suggests its dynamically stable crys-

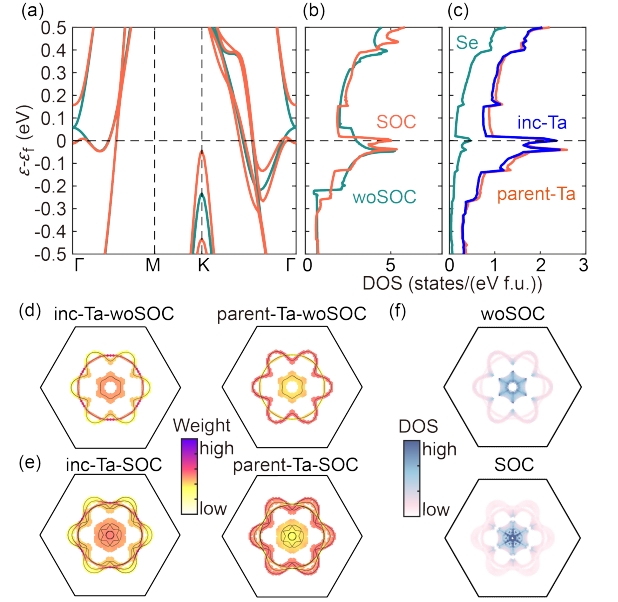


FIG. 6. Electronic structure of $1H_{\text{Ta}}\text{-Ta}_3\text{Se}_4$. Band structures (a) and DOS (b), calculated with and without SOC. (c) Projected DOS onto the electronic states of parent-Ta and inc-Ta atoms, calculated with SOC. Projected electronic states around the Fermi surface onto parent-Ta and inc-Ta atoms, calculated without (d) and with (e) SOC. Only the states within an energy window of ± 35 meV are shown. The solid lines represent the calculated Fermi surface. (f) Visualizations of the contributions to $N(0)$ from the electronic states in BZ, calculated with and without SOC.

tal structure, in contrast to the presence of CDW instabilities in $1H_{\text{hollow}}\text{-Ta}_3\text{Se}_4$ and $2H_{\text{Ta}}\text{-Ta}_3\text{Se}_4$. This indicates the suppression of the 3×3 CDW in $1H\text{-TaSe}_2$ following the intercalation of Ta atoms at the midpoint between each pair of two parent Ta atoms that are vertically aligned in adjacent layers.

To further study the effect of the intercalation on the superconductivity, we tend to the electronic structure. As shown in Fig. 6(a), $1H_{\text{Ta}}\text{-Ta}_3\text{Se}_4$ exhibits a metallic band structure, similar to that of $1H_{\text{hollow}}\text{-}$ and $2H_{\text{Ta}}\text{-Ta}_3\text{Se}_4$. There are several spin-degenerate bands crossing the Fermi level near the Γ point when SOC is not included. This leads to the formation of three Fermi pockets centered at the Γ : a small, hexagonal hole pocket, a circular electron pocket, and a flower-like electron pocket with six petals pointing to the BZ corners. These Fermi pockets are mainly contributed by the hybridization of Ta electrons with different mixing ratio, as shown in Fig. 6(d). The flower-like pocket is primarily contributed by the electronic states of the parent Ta atoms, with a relatively smaller contribution from the intercalated Ta. In contrast, the other two Fermi pockets are mainly associated with the intercalated Ta, with the parent Ta playing a secondary role.

Interestingly, in contrast to the slight increase of $N(0)$

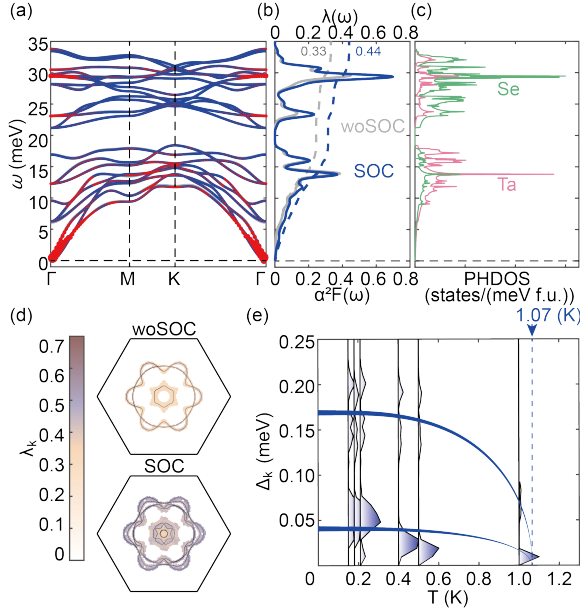


FIG. 7. Calculated properties of $1H_{\text{Ta}}\text{-Ta}_3\text{Se}_4$. (a) $\omega_{\mathbf{q}\nu}$ with (blue) and without (grey) SOC. The size of red dots represent the value of $\lambda_{\mathbf{q}\nu}$ in the presence of SOC. (b) $\alpha^2 F(\omega)$ along with $\lambda(\omega)$, calculated with and without SOC. (c) Projected PHDOS onto the vibrations of Se and Ta atoms. (d) Distribution of \mathbf{k} -resolved EPC constants near the Fermi surface in the presence of SOC. Only the states within an energy window of ± 35 meV are shown. (e) Histograms of $\Delta(\mathbf{k}, T)$ at various temperatures in the presence of SOC. The blue curve represents a BCS fit of the energy gap.

due to SOC in $2H_{\text{Ta}}\text{-Ta}_3\text{Se}_4$ and $1H_{\text{hollow}}\text{-Ta}_3\text{Se}_4$, the $N(0)$ in $1H_{\text{Ta}}\text{-Ta}_3\text{Se}_4$ substantially increases after involving SOC, as shown in Fig. 6(b). This primarily arises from the increased electronic states near the Γ point, where the contribution to $N(0)$ is significantly enhanced, particularly along Γ -M direction, as shown in Fig. 6(f). This results from SOC-induced band splitting at energies slightly above the Fermi level near the Γ point, as shown in Fig. 6(a). The split band is shifted downward to energy levels very close to the Fermi level, exhibiting relatively flat dispersion, which results in the emergence of a peak in the DOS at the Fermi level (Fig. 6(b)). The appearance of the DOS peak increases $N(0)$ from 3.00 /eV/f.u. without SOC to 5.02 /eV/f.u. with SOC included.

The SOC induced $N(0)$ increase is found to be crucial for triggering superconductivity in $1H_{\text{Ta}}\text{-Ta}_3\text{Se}_4$. A comparison of $\lambda_{\mathbf{k}}$ calculated with and without SOC, as depicted in Fig. 7(d), shows an overall enhancement of $\lambda_{\mathbf{k}}$ upon incorporating SOC. This enhancement is physically intuitive, as the rise in $N(0)$ provides a greater number of available channels for EPC. This is also consistent with the computational result, where T_c^{aniso} is calculated to be higher with SOC (1.07 K) compared to without SOC (0.83 K), as shown in Fig. 7(e) and Fig. S10(b) [31], respectively. The calculated $\alpha^2 F(\omega)$

and λ also display consistent results. As the calculated λ increases from 0.33 to 0.44 after SOC is included, as shown in Fig. 7(b). This further confirms the important role of SOC plays in the superconductivity of this system. Therefore, we have shown the SOC-enhanced superconductivity in $1H_{\text{Ta}}\text{-Ta}_3\text{Se}_4$, with comparable value of T_c to TaSe_2 without intercalation, due to substantial increase of electronic states near the Γ point. We also note that, although the $N(0)$ in $1H_{\text{Ta}}\text{-Ta}_3\text{Se}_4$ is significantly higher than that of $1H_{\text{hollow}}\text{-Ta}_3\text{Se}_4$, the EPC λ is slightly lower (0.44 vs 0.64). This discrepancy arises due to the significantly lower $\langle |g|^2 \rangle$, which is 660 meV² in $1H_{\text{Ta}}\text{-Ta}_3\text{Se}_4$ compared to that of 1850 meV² in $1H_{\text{hollow}}\text{-Ta}_3\text{Se}_4$ (see Tab. I).

IV. CONCLUSION AND DISCUSSION

In summary, we have computationally studied the crystal structures, electronic structures, phonons, EPC, and superconductivity of three candidate crystals of Ta_3Se_4 , leading to the following findings.

Firstly, we find rich charge orders in Ta_3Se_4 , arising from the different interlayer stacking between two parent TaSe_2 layers, and intercalation sites being occupied. When the two parent TaSe_2 layers stack in $1H$ order, with the hollow sites being occupied by the intercalants, this leads to the structure of $1H_{\text{hollow}}\text{-Ta}_3\text{Se}_4$, which is observed in experiment. This structure exhibits a $\sqrt{3} \times \sqrt{3}$ CDW, coexisting with superconductivity with an estimated T_c^{aniso} of 1.06 K. The calculated $\sqrt{3} \times \sqrt{3}$ CDW order is in nice agreement with experiment. When the stacking order is $1H$, with the intercalants occupying the sites aligned with the parent Ta atoms in the out-of-plane direction, this leads to the structure of $1H_{\text{Ta}}\text{-Ta}_3\text{Se}_4$. This structure exhibits an absence of CDW, with SOC-enhanced superconductivity, whose T_c^{aniso} is estimated to be 1.07 K. When the stacking order is $2H$, with the intercalants occupying the same sites as $1H_{\text{Ta}}\text{-Ta}_3\text{Se}_4$, this leads to the structure of $2H_{\text{Ta}}\text{-Ta}_3\text{Se}_4$. This structure exhibits a 2×2 CDW, coexisting with superconductivity with an estimated T_c^{aniso} of 1.34 K.

Secondly, in all the three Ta_3Se_4 structures, the parent TaSe_2 layers consistently display suppressed CDW. Meanwhile, the absence, or emergence of new CDW orders in the intercalation layers depends on the interlayer stacking sequences and occupied intercalation sites. In $1H_{\text{hollow}}\text{-Ta}_3\text{Se}_4$, the T_{CDW} is estimated to be 167 K, by considering anharmonicity and quantum fluctuations at finite temperatures, within SSCHA approximation. This T_{CDW} is higher than that of bilayer TaSe_2 . The T_{CDW} is expected to be significantly higher in $2H_{\text{Ta}}\text{-Ta}_3\text{Se}_4$ compared to $1H_{\text{hollow}}\text{-Ta}_3\text{Se}_4$ and bilayer TaSe_2 , based on comparisons of energy gains due to CDW formation, variations in Ta-Ta distances, and phonon energies at the \mathbf{q}_{CDW} among these structures. This suggests that the

self-intercalation in TaSe₂ tends to suppress CDW in parent TaSe₂ layers. Furthermore, the CDWs induced by the self-intercalation in the intercalation layers are enhanced compared to parent TaSe₂.

Thirdly, SOC tends to increase $N(0)$ while simultaneously suppressing EPC matrix elements in Ta₃Se₄ by comparing these quantities across different structures, as tabulated in Tab. I. The interplay between these two competing SOC-induced effects varies among the three Ta₃Se₄ crystal structures, resulting in distinct impacts on their respective T_c^{ME} and T_c^{aniso} . In 1H_{hollow}-Ta₃Se₄, the reduction in EPC matrix elements has a more pronounced impact than the enhancement of $N(0)$, ultimately resulting in a decrease in λ and two types of T_c . In contrast, for 1H_{Ta}-Ta₃Se₄, the $N(0)$ is significantly enhanced due to SOC-induced band splitting. This enhancement results in a substantial increase in $N(0)$ near the Γ point, which provides more available channels for EPC, giving rise to increases in both T_c^{ME} and T_c^{aniso} . The case is different for 2H_{Ta}-Ta₃Se₄, where the influence of SOC on $N(0)$ and EPC matrix elements is minor and tends to cancel out.

Finally, the CDW in 2H_{Ta}-Ta₃Se₄ is found to enhance $N(0)$ relative to its non-CDW phase, primarily attributed to the formation of energy gaps in the occupied states. This unusual behavior distinguishes itself from a typical metal-to-insulator Peierls transition, where energy gaps generally form at the Fermi level.

Our work unveils the properties in self-intercalated bilayer TaSe₂, with a focus on the CDW, superconductivity, magnetism, and proposes candidates for the study of the interplay between these orders.

This work is supported by National Natural Science Foundation of China 11804118, Guangdong Basic and Applied Basic Research Foundation (Grant No.2025A1515010219, 2021A1515010041), and the Science and Technology Planning Project of Guangzhou (Grant No. 202201010222). The Calculations were performed on high-performance computation cluster of Jinan University, and Tianhe Supercomputer System.

All data available from the authors upon reasonable request.

* fpzheng-phy@email.jnu.edu.cn; corresponding author

- [1] H. Zhang, A. Rousuli, K. Zhang, L. Luo, C. Guo, X. Cong, Z. Lin, C. Bao, H. Zhang, S. Xu, *et al.*, Tailored Ising superconductivity in intercalated bulk NbSe₂, *Nature Physics* **18**, 1425 (2022).
- [2] R. Sun, J. Deng, X. Wu, M. Hao, K. Ma, Y. Ma, C. Zhao, D. Meng, X. Ji, Y. Ding, *et al.*, High anisotropy in electrical and thermal conductivity through the design of aerogel-like superlattice (NaOH)_{0.5}NbSe₂, *Nature Communications* **14**, 6689 (2023).
- [3] D. Wu, Y. Lin, L. Xiong, J. Li, T. Luo, D. Chen, and F. Zheng, Enhanced superconductivity in bilayer PtTe₂ by alkali-metal intercalations, *Physical Review B* **103**, 224502 (2021).
- [4] F. Zheng, X.-B. Li, P. Tan, Y. Lin, L. Xiong, X. Chen, and J. Feng, Emergent superconductivity in two-dimensional NiTe₂ crystals, *Physical Review B* **101**, 100505 (2020).
- [5] T. Agarwal, C. Patra, A. Kataria, R. R. Chowdhury, and R. Singh, Quasi-two-dimensional anisotropic superconductivity in Li-intercalated 2H-TaS₂, *Physical Review B* **107**, 174509 (2023).
- [6] H. Liu, S. Huangfu, X. Zhang, H. Lin, and A. Schilling, Superconductivity and charge density wave formation in lithium-intercalated 2H-TaS₂, *Physical Review B* **104**, 064511 (2021).
- [7] X. Fan, H. Chen, L. Zhao, S. Jin, and G. Wang, Quick suppression of superconductivity of NbSe₂ by Rb intercalation, *Solid State Communications* **297**, 6 (2019).
- [8] C. Hong, D. Wu, X.-B. Li, and F. Zheng, Multigap superconductivity in lithium intercalated bilayer Mo₂C, *Physical Review B* **109**, 064515 (2024).
- [9] J. A. Woollam and R. B. Somoano, Physics and chemistry of MoS₂ intercalation compounds, *Materials Science and Engineering* **31**, 289 (1977).
- [10] G. Huang, Z. Xing, and D. Xing, Dynamical stability and superconductivity of Li-intercalated bilayer MoS₂: A first-principles prediction, *Physical Review B* **93**, 104511 (2016).
- [11] J. K. Ellis, M. J. Lucero, and G. E. Scuseria, The indirect to direct band gap transition in multilayered MoS₂ as predicted by screened hybrid density functional theory, *Applied physics letters* **99**, 261908 (2011).
- [12] X.-K. Wei, A. R. Jalil, P. Rüßmann, Y. Ando, D. Grützmacher, S. Blügel, and J. Mayer, Atomic diffusion-induced polarization and superconductivity in topological insulator-based heterostructures, *ACS Nano* **18**, 571 (2024).
- [13] F. Wang, Y. Zhang, Z. Wang, H. Zhang, X. Wu, C. Bao, J. Li, P. Yu, and S. Zhou, Ionic liquid gating induced self-intercalation of transition metal chalcogenides, *Nature Communications* **14**, 4945 (2023).
- [14] X. Zhao, P. Song, C. Wang, A. C. Riis-Jensen, W. Fu, Y. Deng, D. Wan, L. Kang, S. Ning, J. Dan, *et al.*, Engineering covalently bonded 2D layered materials by self-intercalation, *Nature* **581**, 171 (2020).
- [15] S. Pan, M. Hong, L. Zhu, W. Quan, Z. Zhang, Y. Huan, P. Yang, F. Cui, F. Zhou, J. Hu, F. Zheng, and Y. Zhang, On-Site Synthesis and Characterizations of Atomically-Thin Nickel Tellurides with Versatile Stoichiometric Phases through Self-Intercalation, *ACS Nano* **16**, 11444 (2022).
- [16] Q. Yang, K. Wang, M. Zhang, F. Du, J. Li, C. Zheng, and J. Li, Advancements in synthetic and electrocatalytic exploitation of guest-host intercalated 2D materials, *Progress in Natural Science: Materials International* **34**, 454 (2024).
- [17] Q. He, K. Si, Z. Xu, X. Wang, C. Jin, Y. Yang, J. Wei, L. Meng, P. Zhai, P. Zhang, P. Tang, and Y. Gong, Direct synthesis of controllable ultrathin heteroatoms-intercalated 2D layered materials, *Nature Communications* **15**, 6320 (2024).
- [18] F. D. S. J.A. Wilson and S. Mahajan, Charge-density waves and superlattices in the metallic layered transition metal dichalcogenides, *Advances in Physics* **24**, 117

TABLE I. The parameters of each structure, where the $N(0)$ is given in units of $/\text{eV}/\text{c.f.}$, the T_c and ω_{log} is given in units of K. The averaged EPC matrix element square, $\langle |g|^2 \rangle = 1/N(0) \int \alpha^2 F(\omega) d\omega$, is in the unit of 10^3 meV^2 . The data in parentheses are calculated without SOC.

System	CDW	$N(0)$	$\langle g ^2 \rangle$	ω_{log}	λ	T_c^{ME}	T_c^{aniso}	Exp. T_c
Bulk ^a	3×3	2.8		202.73	0.4	0.14		0.1–0.15
2H-TaSe ₂ multilayer ^b								1–1.4
monolayer ^c	3×3	2.46		79.07	0.71	1.8		
Ta ₃ Se ₄ ^d	$1H_{\text{hollow}}$	$\sqrt{3} \times \sqrt{3}$	1.98 (1.65)	1.85 (2.82)	110.92 (84.64)	0.64 (0.92)	1.79 (3.82)	1.06 (7.79)
	$2H_{\text{Ta}}$	2×2	2.46 (2.17)	1.24 (1.45)	109.06 (121.13)	0.48 (0.47)	0.39 (0.42)	(1.34)
	$1H_{\text{Ta}}$	none	5.02 (3.00)	0.66 (0.87)	134.68 (150.44)	0.44 (0.33)	0.27 (0.01)	1.07 (0.83)

^a The experimental data are from [18–20], and the computational data are from [81].

^b The experimental data are from [57, 82].

^c The computational data are from [81, 83].

^d This work.

- (1975).
- [19] D. Bhoi, S. Khim, W. Nam, B. Lee, C. Kim, B.-G. Jeon, B. Min, S. Park, and K. H. Kim, Interplay of charge density wave and multiband superconductivity in 2H-Pd_xTaSe₂, *Scientific reports* **6**, 24068 (2016).
- [20] D. Freitas, P. Rodière, M. Osorio, E. Navarro-Moratalla, N. Nemes, V. Tissen, L. Cario, E. Coronado, M. García-Hernández, S. Vieira, *et al.*, Strong enhancement of superconductivity at high pressures within the charge-density-wave states of 2H-TaS₂ and 2H-Pd_xTaSe₂, *Physical Review B* **93**, 184512 (2016).
- [21] D. E. Moncton, J. D. Axe, and F. J. DiSalvo, Study of Superlattice Formation in 2H-NbSe₂ and 2H-TaSe₂ by Neutron Scattering, *Phys. Rev. Lett.* **34**, 734 (1975).
- [22] A. C. Neto, Charge density wave, superconductivity, and anomalous metallic behavior in 2D transition metal dichalcogenides, *Physical review letters* **86**, 4382 (2001).
- [23] J. Dai, E. Calleja, J. Alldredge, X. Zhu, L. Li, W. Lu, Y. Sun, T. Wolf, H. Berger, and K. McElroy, Microscopic evidence for strong periodic lattice distortion in two-dimensional charge-density wave systems, *Physical Review B* **89**, 165140 (2014).
- [24] G. Kresse and D. Joubert, From ultrasoft pseudopotentials to the projector augmented-wave method, *Phys. Rev. B* **59**, 1758 (1999).
- [25] D. Vanderbilt, Soft self-consistent pseudopotentials in a generalized eigenvalue formalism, *Physical Review B* **41**, 7892–7895 (1990).
- [26] J. P. Perdew, A. Ruzsinszky, G. I. Csonka, O. A. Vydrov, G. E. Scuseria, L. A. Constantin, X. Zhou, and K. Burke, Restoring the density-gradient expansion for exchange in solids and surfaces, *Phys. Rev. Lett.* **100**, 136406 (2008).
- [27] S. Baroni, S. de Gironcoli, A. Dal Corso, and P. Giannozzi, Phonons and related crystal properties from density-functional perturbation theory, *Rev. Mod. Phys.* **73**, 515 (2001).
- [28] F. Giustino, Electron-phonon interactions from first principles, *Rev. Mod. Phys.* **89**, 015003 (2017).
- [29] P. Giannozzi, S. Baroni, N. Bonini, M. Calandra, R. Car, C. Cavazzoni, D. Ceresoli, G. L. Chiarotti, M. Cococcioni, I. Dabo, A. D. Corso, S. de Gironcoli, S. Fabris, G. Fratesi, R. Gebauer, U. Gerstmann, C. Gougoussis, A. Kokalj, M. Lazzeri, L. Martin-Samos, N. Marzari, F. Mauri, R. Mazzarello, S. Paolini, A. Pasquarello, L. Paulatto, C. Sbraccia, S. Scandolo, G. Sclauzero, A. P. Seitsonen, A. Smogunov, P. Umari, and R. M. Wentzcovitch, QUANTUM ESPRESSO: a modular and open-source software project for quantum simulations of materials, *Journal of Physics: Condensed Matter* **21**, 395502 (2009).
- [30] G. Kresse and J. Furthmüller, Efficient iterative schemes for ab initio total-energy calculations using a plane-wave basis set, *Phys. Rev. B* **54**, 11169 (1996).
- [31] Supplemental Material. The Supplemental Material also contains Refs. [32–48].
- [32] A. Dal Corso, Pseudopotentials periodic table: From h to pu, *Computational Materials Science* **95**, 337 (2014).
- [33] G. Prandini, A. Marrazzo, I. E. Castelli, N. Mounet, and N. Marzari, Precision and efficiency in solid-state pseudopotential calculations, *npj Computational Materials* **4**, 72 (2018).
- [34] W. Kohn and L. J. Sham, Self-consistent equations including exchange and correlation effects, *Phys. Rev.* **140**, A1133 (1965).
- [35] D. R. Hamann, M. Schlüter, and C. Chiang, Norm-conserving pseudopotentials, *Phys. Rev. Lett.* **43**, 1494 (1979).
- [36] J. P. Perdew, K. Burke, and M. Ernzerhof, Generalized gradient approximation made simple, *Phys. Rev. Lett.* **77**, 3865 (1996).
- [37] D. R. Hamann, Optimized norm-conserving Vanderbilt pseudopotentials, *Phys. Rev. B* **88**, 085117 (2013).
- [38] M. Schlipf and F. Gygi, Optimization algorithm for the generation of ONCV pseudopotentials, *Comput. Phys. Commun.* **196**, 36 (2015).
- [39] K. F. Garrity, J. W. Bennett, K. M. Rabe, and D. Vanderbilt, Pseudopotentials for high-throughput dft calculations, *Computational Materials Science* **81**, 446 (2014).
- [40] S. Grimme, Semiempirical gga-type density functional constructed with a long-range dispersion correction, *Journal of Computational Chemistry* **27**, 1787 (2006).
- [41] S. Grimme, J. Antony, S. Ehrlich, and H. Krieg, A consistent and accurate ab initio parametrization of density functional dispersion correction (dft-d) for the 94 elements h-pu, *The Journal of Chemical Physics* **132**, 154104 (2010).
- [42] M. Dion, H. Rydberg, E. Schröder, D. C. Langreth, and B. I. Lundqvist, Van der waals density functional for general geometries, *Phys. Rev. Lett.* **92**, 246401 (2004).
- [43] K. Lee, E. D. Murray, L. Kong, B. I. Lundqvist, and

- D. C. Langreth, Higher-accuracy van der waals density functional, *Phys. Rev. B* **82**, 081101 (2010).
- [44] J. c. v. Klimeš, D. R. Bowler, and A. Michaelides, Van der waals density functionals applied to solids, *Phys. Rev. B* **83**, 195131 (2011).
- [45] K. Berland and P. Hyldgaard, Exchange functional that tests the robustness of the plasmon description of the van der waals density functional, *Phys. Rev. B* **89**, 035412 (2014).
- [46] I. Hamada, van der waals density functional made accurate, *Phys. Rev. B* **89**, 121103 (2014).
- [47] I. Hamada and M. Otani, Comparative van der waals density-functional study of graphene on metal surfaces, *Phys. Rev. B* **82**, 153412 (2010).
- [48] V. R. Cooper, Van der waals density functional: An appropriate exchange functional, *Phys. Rev. B* **81**, 161104 (2010).
- [49] I. Souza, N. Marzari, and D. Vanderbilt, Maximally localized wannier functions for entangled energy bands, *Phys. Rev. B* **65**, 035109 (2001).
- [50] N. Marzari and D. Vanderbilt, Maximally localized generalized wannier functions for composite energy bands, *Phys. Rev. B* **56**, 12847 (1997).
- [51] A. A. Mostofi, J. R. Yates, Y.-S. Lee, I. Souza, D. Vanderbilt, and N. Marzari, wannier90: A tool for obtaining maximally-localised wannier functions, *Computer Physics Communications* **178**, 685 (2008).
- [52] S. Poncé, E. Margine, C. Verdi, and F. Giustino, EPW: Electron-phonon coupling, transport and superconducting properties using maximally localized wannier functions, *Computer Physics Communications* **209**, 116 (2016).
- [53] M. Alidoosti, D. N. Esfahani, and R. Asgari, Charge density wave and superconducting phase in monolayer InSe, *Phys. Rev. B* **103**, 035411 (2021).
- [54] P. B. Allen and R. C. Dynes, Transition temperature of strong-coupled superconductors reanalyzed, *Phys. Rev. B* **12**, 905 (1975).
- [55] C.-S. Lian, C. Si, and W. Duan, Single anisotropic gap superconductivity and proximity effect in PbTaSe_2 , *Phys. Rev. B* **100**, 235420 (2019).
- [56] T. Luo, M. Zhang, J. Shi, and F. Zheng, Emergent charge density wave featuring quasi-one-dimensional chains in Ta-intercalated bilayer $2H\text{-TaS}_2$ with coexisting superconductivity, *Physical Review B* **107**, L161401 (2023).
- [57] Y. Wu, J. He, J. Liu, H. Xing, Z. Mao, and Y. Liu, Dimensional reduction and ionic gating induced enhancement of superconductivity in atomically thin crystals of $2H\text{-TaSe}_2$, *Nanotechnology* **30**, 035702 (2018).
- [58] E. R. Margine, and F. Giustino, Anisotropic Migdal-Eliashberg theory using wannier functions, *Phys. Rev. B* **87**, 024505 (2013).
- [59] I. Errea, M. Calandra, and F. Mauri, Anharmonic free energies and phonon dispersions from the stochastic self-consistent harmonic approximation: Application to platinum and palladium hydrides, *Phys. Rev. B* **89**, 064302 (2014).
- [60] A. Slimani, H. Khemakhem, and K. Boukheddaden, Structural synergy in a core-shell spin crossover nanoparticle investigated by an electroelastic model, *Phys. Rev. B* **95**, 174104 (2017).
- [61] L. Monacelli, R. Bianco, M. Cherubini, M. Calandra, I. Errea, and F. Mauri, The stochastic self-consistent harmonic approximation: calculating vibrational properties of materials with full quantum and anharmonic effects, *Journal of Physics: Condensed Matter* **33**, 363001 (2021).
- [62] L. Zhang, J. Han, H. Wang, R. Car, and W. E, Deep potential molecular dynamics: A scalable model with the accuracy of quantum mechanics, *Phys. Rev. Lett.* **120**, 143001 (2018).
- [63] H. Wang, L. Zhang, J. Han, and W. E, DeePMD-kit: A deep learning package for many-body potential energy representation and molecular dynamics, *Computer Physics Communications* **228**, 178 (2018).
- [64] F. Zheng, Z. Zhou, X. Liu, and J. Feng, First-principles study of charge and magnetic ordering in monolayer NbSe_2 , *Physical Review B* **97**, 081101 (2018).
- [65] F. Zheng and J. Feng, Electron-phonon coupling and the coexistence of superconductivity and charge-density wave in monolayer NbSe_2 , *Physical Review B* **99**, 161119 (2019).
- [66] B. E. Brown and D. J. Beerntsen, Layer structure polytypism among niobium and tantalum selenides, *Acta Crystallographica* **18**, 31 (1965).
- [67] J.-A. Yan, M. A. D. Cruz, B. Cook, and K. Varga, Structural, electronic and vibrational properties of few-layer $2H\text{-}$ and $2T\text{-TaSe}_2$, *Scientific reports* **5**, 1 (2015).
- [68] Y. Ge and A. Y. Liu, Effect of dimensionality and spin-orbit coupling on charge-density-wave transition in $2H\text{-TaSe}_2$, *Physical Review B* **86**, 104101 (2012).
- [69] J. Si, M. Wei, H. Wu, R. Xiao, and W. Lu, Charge-density-wave tuning in monolayer $1H\text{-TaSe}_2$ by biaxial strain and charge doping, *Europhysics Letters* **127**, 37001 (2019).
- [70] C.-S. Lian, C. Heil, X. Liu, C. Si, F. Giustino, and W. Duan, Intrinsic and doping-enhanced superconductivity in monolayer $1H\text{-TaS}_2$: Critical role of charge ordering and spin-orbit coupling, *Physical Review B* **105**, L180505 (2022).
- [71] M. Lawan Adam, I. Buba Garba, A. Alhaji Bala, A. Aji Suleiman, S. Muhammad Gana, and F. Lawan Adam, Tuning superconductivity and charge density wave order in TaSe_2 through Pt intercalation, *Physical Review B* **107**, 104510 (2023).
- [72] W. Wan, R. Harsh, P. Dreher, F. de Juan, and M. M. Ugeda, Superconducting dome by tuning through a van Hove singularity in a two-dimensional metal, *npj 2D Materials and Applications* **7**, 41 (2023).
- [73] H. Paudyal and E. R. Margine, Superconducting properties in doped $2M\text{-WS}_2$ from first principles, *Journal of Materials Chemistry C* **10**, 7917 (2022).
- [74] Y. Q. Fang, D. Wang, W. Zhao, and F. Q. Huang, Large magnetoresistance in the monoclinic $2M\text{-WSe}_2$, *Europhysics Letters* **131**, 10005 (2020).
- [75] S. Piscanec, M. Lazzeri, F. Mauri, A. C. Ferrari, and J. Robertson, Kohn anomalies and electron-phonon interactions in graphite, *Phys. Rev. Lett.* **93**, 185503 (2004).
- [76] J. Shi, X. Chen, L. Zhao, Y. Gong, M. Hong, Y. Huan, Z. Zhang, P. Yang, Y. Li, Q. Zhang, *et al.*, Chemical vapor deposition grown wafer-scale 2D tantalum diselenide with robust charge-density-wave order, *Advanced Materials* **30**, 1804616 (2018).
- [77] H. Ryu, Y. Chen, H. Kim, H.-Z. Tsai, S. Tang, J. Jiang, F. Liou, S. Kahn, C. Jia, A. A. Omrani, *et al.*, Persistent charge-density-wave order in single-layer TaSe_2 , *Nano letters* **18**, 689 (2018).
- [78] W. Wang, K. Zhang, Y. Liu, A. Li, J. Li, and C. Si, Polymorphic charge density waves, magnetism, and topolo-

- gies in $1T'$ -TaTe₂, *Physical Review B* **109**, 104107 (2024).
- [79] D. Dangić, L. Monacelli, R. Bianco, F. Mauri, and I. Errea, Large impact of phonon lineshapes on the superconductivity of solid hydrogen, *Communications Physics* **7**, 150 (2024).
 - [80] D. Lin, S. Li, J. Wen, H. Berger, L. Forró, H. Zhou, S. Jia, T. Taniguchi, K. Watanabe, X. Xi, and M. Bahramy, Patterns and driving forces of dimensionality-dependent charge density waves in $2H$ -type transition metal dichalcogenides, *Nature Communications* **11**, 2406 (2020).
 - [81] C.-S. Lian, C. Heil, X. Liu, C. Si, F. Giustino, and W. Duan, Coexistence of superconductivity with enhanced charge density wave order in the two-dimensional limit of TaSe₂, *The Journal of Physical Chemistry Letters* **10**, 4076 (2019).
 - [82] J. Galvis, P. Rodiere, I. Guillamon, M. Osorio, J. G. Rodrigo, L. Cario, E. Navarro-Moratalla, E. Coronado, S. Vieira, and H. Suderow, Scanning tunneling measurements of layers of superconducting $2H$ -TaSe₂: Evidence for a zero-bias anomaly in single layers, *Physical Review B* **87**, 094502 (2013).
 - [83] C.-S. Lian, Interplay of charge ordering and superconductivity in two-dimensional $2H$ group V transition-metal dichalcogenides, *Physical Review B* **107**, 045431 (2023).
 - [84] C. van Efferen, J. Berges, J. Hall, E. van Loon, S. Kraus, A. Schobert, T. Wekking, F. Huttmann, E. Plaar, N. Rothenbach, K. Ollefs, L. M. Arruda, N. Brookes, G. Schönhoff, K. Kummer, H. Wende, T. Wehling, and T. Michely, A full gap above the Fermi level: the charge density wave of monolayer VS₂, *Nature Communications* **12**, 6837 (2021).